Unraveling Fullerene-Perovskite Interactions Introduces Advanced Blend Films for Performance-Improved Solar Cells

Jorge Pascual,[a,b,c] Silvia Collavini,[a] Sebastian F. Völker,[a] Nga Phung,[c] Elisa Palacios-Lidon,[d] Lourdes Irusta,[a] Hans-Jürgen Grande,[b] Antonio Abate,[c] Juan Luis Delgado,*[a,e] Ramón Tena-Zaera*[b]

Fullerenes have become one of the most interesting families of molecules to be used in perovskite solar cells. A wide range of derivatives have been designed and applied in this type of devices due to their ability to passivate defects. However, the relevance of these functionalizations on device performance is not clear yet, as there might be perovskite-fullerene interactions yet to be figured out. In this work a new set of spectroscopical techniques is proposed for the identification of perovskite:fullerene complexes that could be generated in solution, focusing on the non-covalent interactions taking part. The obtained results allow understanding the importance of a suitable chemical modification of fullerenes and the implications that the functional group has in the thin film scenario. Taking advantage of the gained knowledge, a new fullerene with optimized structure, FU11, is synthesized and applied in blend films with perovskite, achieving efficiencies of up to 18.3% and universality of this technique for different cell configurations. Furthermore, a clear correlation can be observed between the ability of the fullerene to coordinate perovskite and the final solar cell performance.

Introduction

The big growth that photovoltaic (PV) field has experienced in the last years is certainly unquestionable, and the impact of the discovery of perovskite solar cells (PSC) on this cannot be taken for granted. These photovoltaic devices have experienced a quick development from their initial 3.8% in 2009[1] to their current 23.7% in 2018[2]. This outstanding progress is due to their high versatility for processing and chemical compatibility with a broad range of compounds, such as carbon nanomaterials as semiconductors for hole-(HTLs) or electron-transporting layers (ETLs).[3] In particular, fullerenes have been prominent players in the development of this technology due to their unique physicochemical properties.[4-8] Extendedly applied as charge-transporting materials,[9-19] mainly as electron-selective ones, and additives in the perovskite layer,[21-28] these carbon allotropes have provided plenty of benefits to this type of PV devices. Improvements in fill factor (FF)[25,26,27] stability[21,23,25,26,30] and hysteresis suppression[22-25,31-33] have been supported on the different roles of fullerenes in perovskite devices. One of their fundamental properties is the ability for passivating trap states as they can bind uncoordinated atoms at the grain boundaries, as it has been widely claimed by several research groups.[14-19,25,26,29] Their chemical nature (e.g. symmetry, non-polarity, spherical shape) has also made them perfect candidates as frames for the growth of perovskite crystals, leading to improved morphologies and increased grain sizes.[34] In fact, due to their high chemical versatility, a wide range of fullerene derivatives could be successfully produced and applied in PSCs, leading to devices with improved performance.[22-28] Nevertheless, if fullerenes are to be used in future protocols for PSC design, structurally-optimized fullerene derivatives would be required, therefore being still plenty of room for improvement in the understanding of the perovskite:fullerene systems and the relevance of the fullerene nature.

Further insights on the physicochemical implications of fullerenes in perovskite would allow designing new generation fullerenes with advanced properties, and shed light on current issues like the origin of FF increase or hysteresis suppression. In this sense, there is need for further understanding on the characteristics of perovskite-fullerene blends. A simple and straightforward approach that could shed light on this subject would be the study of these systems from their solution state to the device scenario with spectroscopical techniques, taking a look at all the interactions playing a role in solution and their effects on layer and device physico-chemical properties. In this respect, various spectroscopic techniques have already been applied separately for the study of certain perovskite formulations, not yet with fullerenes. In particular, Fourier-transform infrared spectroscopy (FTIR) has been extendedly used for the evaluation of the bonds that are being broken and established in the perovskite complex formation between the different precursors.[35-41] Not only that but ^{1}H-NMR was also applied in the work by Yavary and co-workers for understanding the chemical role of carbon nanoparticles in perovskite solutions.[42]

Considering fullerenes, their electronegative nature is particularly relevant for understanding how they would behave in a blend together with perovskite. In fact, this characteristic was found as critical to explain one of the most recent findings in perovskite:fullerene systems by Gharibzadeh and colleagues, who proved the injection of electrons from the perovskite to C_{70} in the picoseconds scale.[43] With the addition of a molecule being able to accept electrons like this fullerene they managed to decrease the trap density of the perovskite layer, which led to a record power conversion efficiency (PCE) of 15.7% for ETL-free devices. This chemical nature strongly influences their chemical compatibility and thus the species, which they will preferentially bind, being reported studies completely coherent with this. In this sense, several works have proved the establishment of intermolecular bonds between arenes and anions through anion-π interactions[44-49] and, more in particular, between fullerenes and halides.[22,33,50,51] This finding suggests that fullerenes would show certain preference towards halide-rich sites in the perovskite film and, in this line, Xu and co-workers found out the passivating role of [6,6]-phenyl C_{61} butyric acid methyl ester (PCBM) for Pb-I antisites in the

perovskite layer while studying the anion-π interaction.[22] Taking into account the ability of fullerenes to interact with perovskite, studying these interactions and how to modulate them would open a wide range of possibilities for the design, synthesis and application of new fullerenes with optimized structure for the enhancement of certain properties such as defect passivation.

Herein, we report evidence on the formation of specific interactions between fullerenes and perovskite precursors. To prove this fact, a novel combination of spectroscopic techniques was used on perovskite precursor solutions doped with fullerenes of different structural nature. NMR and IR spectra provided insightful data on the atoms involved in the new complex formed. The alterations generated by the insertion of fullerenes were later linked to microstructural properties (i.e. characterized by atomic force microscopy (AFM)) of the perovskite layer. To further confirm the benefits of fullerene addition to PSCs, devices of various configurations were fabricated, all of them suggesting the FF as the main source of improvement in the performance. Furthermore, based on the chemical knowledge on perovskite:fullerene mixtures, a novel fullerene was synthesized, which led to PSCs of improved performance with PCE values up to 18.3%.

Results and discussion

Considering the currently open questions around the influence of perovskite-fullerene interactions on the device performance, we decided to study the relevance of structural characteristics of fullerenes on this by different spectroscopic methods. Therefore, we focused the analysis on certain selected fullerenes for a suitable comparison. In particular, we decided to study the specific cases of **IS2**, a fullerene functionalized with an isoxazoline group, and the non-functionalized C_{60} and C_{70}. This molecule, particularly appealing as it provided the highest efficiencies for ETL-free devices,[28] holds a characteristic functionalization that could help understanding possible working mechanisms. Since **IS2** contains fluorine atoms, we decided to perform ^{19}F-NMR experiments on 4:1 dimethylformamide:dimethyl sulfoxide (DMF:DMSO) . As it can be seen in Figure 1a, the five fluorine atoms of this material show up only in three different signals (F_A at 161.0 ppm, F_B at 138.9 ppm and F_C at 150.0 ppm), where the fluorine atoms in *ortho* and *meta* positions F_A and F_B integrate both for two fluorine atoms due to their magnetic equivalence. Nevertheless, when the same experiment was carried out in the presence of $MA_{0.15}FA_{0.85}PbBr_{0.15}I_{0.85}$ (MAFA perovskite, where MA and FA stand for methylammonium and formamidinium, respectively) perovskite solution, the three signals were split into five, changing the relative values of what they integrate for. In the first case where **IS2** is alone in solution, both sides of the aromatic ring are magnetically equivalent, explaining the integration for each of the fluorine atoms. However, the presence of perovskite precursors in solution suppresses this equivalency and new signals are found. The origin of these could be due to the fact that new chemical species is being formed, in which the shift and multiplicity of the NMR signals is therefore altered. One possible explanation could be the formation of hydrogen bonds between the N or O atoms of the **IS2** isoxazoline, which could act as Lewis bases, and perovskite amine or lead iodide (Figure 1b). Due to the existence of a new non-coordinative bond through the isoxazoline moiety, the atoms in the aromatic ring would experience stronger electronic repulsions coming from the coordinating perovskite precursors. Therefore, the magnetic environment of fluorine atoms is changed, and so their chemical shift in the NMR spectrum. This hypothesis is also supported by the fact that fluorine atom in *para* position F_C at 150.0 ppm is the less affected one in the aromatic ring, as it would be the furthest one in space from this potential coordinative bond.

These results point out the presence of some kind of interaction between the fullerene and perovskite precursors, but not specific bond formations. In order to tackle this issue, we thought of trying the same experiment but with each perovskite precursor individually (i.e., **IS2**:FAI and **IS2**:PbI2). The ^{19}F-NMR spectra in Fig. S1 show that the 3 signals remained unchanged for all of these solutions. This finding suggests that **IS2** might not be forming any complex with each precursor separately, as it might only participate in the complete perovskite complex.

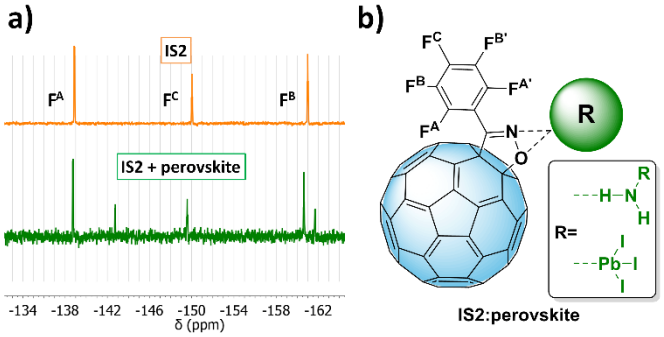

Fig. 1. a) ^{19}F-NMR spectrum of **IS2**-saturated DMF:DMSO (4:1) solution with and without MAFA (1.2 M) perovskite; b) Scheme of potential complexes to be formed between **IS2** and perovskite precursors.

Trying to find some kind of evidence on the bonds being formed between fullerenes and perovskite, solutions of $MAPbI_3$ (MAPI) at 1.2 M in DMSO with C_{60}, C_{70} and **IS2** were analyzed by FTIR spectroscopy means. This also represents the first study of perovskite complexes in solution by FTIR means, as every study done so far involved the preparation of perovskite powders. Due to the wide-absorbing range of the solvent (DMSO) in IR, N-H stretching vibration was the only character that could be studied, which typically appears in the 3500-3000 cm^{-1} region. As it can be seen in Fig. 2a, the band for MAPI:C_{60} and MAPI:C_{70} remained in a comparable situation to the original pristine MAPI at 3145 cm^{-1}, but for **IS2** the band widened and shifted to higher wavenumber values (3164 cm^{-1}). The widening of the signal is a sign of the formation of H-bonds, potentially coming from fullerene-MA interactions. However, the shift of the N-H stretching vibration to higher energy values means that the N-H bond is stronger, what could mean that the potential H-bond between **IS2** and the amine would be weaker than the original one in the perovskite. Nevertheless, both shift and widening of the N-H signal point out the existence of **IS2**-perovskite interactions that do not

happen for the rest of the fullerenes. Additionally, these two phenomena (i.e. shift and widening) were not observed when studying MAI solutions in the presence of these fullerenes (Fig. S2). The spectra were identical for every MAI and MAI-fullerene solution, stressing out that fullerenes and methylammonium do not establish any interaction when PbI_2 is not in solution, even for the case of **IS2**. Overall, these results point in the same direction as the ones obtained by ^{19}F-NMR spectroscopy in Fig. 1 and S1, as an interaction between **IS2** and perovskite can be observed, but only in the presence of the full perovskite complex. Additionally, FTIR shows for the first time the formation of H-bonds between functionalized fullerenes and perovskite amines, which might be the role of the Lewis bases that they hold.

In order to further study the perovskite amine precursor, ^{1}H-NMR experiments were carried out to perovskite solution together with the studied fullerenes. Fig. S3 shows how protons at 8.9 ppm belonging to FA were deshielded and split into higher multiplicities, independently of the fullerene nature. This splitting could only be seen for the protons belonging to FA and not for MA, due to the structure of the first one. FA protons can be differentiated in the shift value as there are two amine moieties in the same molecule, while MA contains only one, and the protonated form has resonance structures that hinder free rotation of C-N bonds. Following the same line as the previous experiments, when solutions without PbI_2 were measured (i.e. FAI:fullerenes), the effect of fullerenes vanished once again, showing in every case unaffected FA protons (Fig. S4). However, C_{60} and C_{70} lack of any functionalization that would allow them establishing any H-bond with perovskite amine groups. Therefore, fullerenes might have some influence on perovskite amine groups in an indirect way, probably through the establishment of anion-π coordinative bonds between the fullerene cage and iodide from PbI_2 in the perovskite complex. As pointed out earlier, this kind of bond has been characterized in the literature for very diverse arene-anion systems,[44-49] including fullerenes.[22,33,50,51]

In order to test the strength of the complexes that might be forming between perovskite and the different fullerenes, we decided to add a small fraction of toluene to mixtures with perovskite:fullerene complexes. This is a solvent with high affinity to other non-polar molecules such as fullerenes; therefore we could expect toluene molecules to solvate fullerenes and, in turn, the complex to be broken, while monitoring all these changes by NMR. In this sense, the MAFA:fullerene solutions showed in Fig. S3 were analyzed again by ^{1}H-NMR after the addition to the of a ¼ fraction of toluene-d8. As shown in Fig. 2b, for the non-substituted fullerenes C_{60} and C_{70} the splitting of the protons of FAI that the fullerene causes was no longer seen, whilst it remained for isoxazoline fullerene **IS2**. These results point to the formation of a stronger complex with the perovskite when the fullerene has a second binding group such as the isoxazoline, as it does not disassemble when an aromatic co-solvent is added. In fact, all acquired spectroscopic data points out coherently the ability of functionalized fullerenes to form two-sided complexes with perovskite, suggesting that non-functionalized C_{60} and C_{70} participate in the perovskite complex just through anion-π bonds with PbI_2 (Fig. 2c), whilst the ones with Lewis base functional groups (**IS2**) can also establish H-bonds with perovskite amines (Fig. 2d), leading to stronger complexes. It must be stressed out that Fig. 2c and 2d are a tentative structural representation of the interactions under study and do not belong to a claim of an exact perovskite-fullerene complex structure.

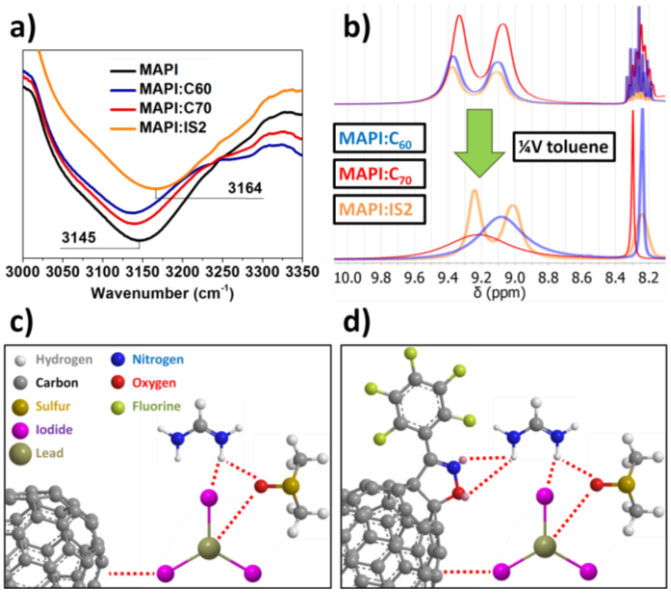

Fig. 2. a) FTIR spectra of MAPI perovskite solution (1.2 M) and containing C_{60}, C_{70} and **IS2**; b) ^{1}H-NMR spectra of MAFA perovskite solution (1.2 M) containing C_{60}, C_{70} and **IS2** and after the addition of ¼ parts of toluene-d8; c) Tentative structural explanation of the interactions undergoing in the perovskite complexes with non-functionalized fullerenes and d) functionalized fullerenes.

Considering these results, we believe that the chemical implications of using fullerenes in perovskite solutions and the effect of fullerene nature were now better understood. The ability of **IS2** to coordinate perovskite more strongly was proven, confirming the great potential of isoxazoline group in fullerene derivatives. Nevertheless, the outcome of forming these complexes in perovskite films and devices was still unclear. To address this issue, we first designed a fullerene derivative for optimized performance. We thought on a fullerene structure resulting from the combination of the most successful molecules in previous studies for ETL-free PSCs, C_{70}[21] (Fig. 3a) and **IS2**,[28] hoping for a synergistic structural effect. The resulting fullerene **FU11** (Fig. 3b) is a C_{70}-cored **IS2** analogue, thus holding the same isoxazoline group. **FU11** was synthesized (Scheme S1) and fully characterized by ^{13}C and ^{19}F-NMR spectroscopies (Fig. S5-6), mass spectroscopy (Fig. S7), UV-vis spectroscopy (Fig. S8) and cyclic voltammetry (Fig. S9). This novel fullerene material was subjected to the same spectroscopic techniques used for **IS2**, and indeed behaved in a similar way, showing the same trend, for ^{1}H-NMR (with and without toluene-d8, Fig. S10-12) and FTIR (Fig. S13-14). In the case of ^{19}F-NMR analysis we could not observe well resolved fluorine signals (Fig. S15). This can be explained by the fact that C_{70} derivatives are not a unique molecule but a mixture of various regioisomers, showing different NMR patterns. Thus, its suitable detection and assignment by ^{19}F-NMR is more complicated than in the case of **IS2**. This is an issue to deal with when working with C_{70} derivatives, widely reported in literature.[53-54]

With the new fullerene **FU11** synthesized, we were now able to compare this structurally-optimized fullerene with its non-functionalized analogue, C_{70}. We started preparing perovskite films

out of MAPI:fullerene solutions and the resulting layers were characterized by AFM means. Even if at the initial measurements stages the two fullerenes thin films are essentially similar (Fig. S16), the surface chemistry-sensitive phase images reveal a strong time-evolution divergence depending of the fullerene type, as shown in Fig. 3c and 3d. For the C_{70}- containing perovskite films, the gradual increase of the phase signal can be correlated with the C_{70} diffusion to the surface (Fig. 3c).[55] On the contrary, this effect is absent in layers containing **FU11**, that remain stable over time (Fig. 3d). Similar measurements in far apart regions of the same sample lead to a completely reproducible behaviour: that is, similar initial state and a C_{70} diffusion towards the surface with time. Hence, we conclude that the C_{70} diffusion is induced by the AFM itself and is probably due to the local surface heating by the AFM red laser used in the beam deflection detection. A potential C_{70} migration from the film bulk to the surface that does not happen for **FU11** might be related to the strength with which each of these fullerenes bind to the perovskite. While **FU11** could have two binding spots to perovskite in its structure as proposed previously, this is not the case for C_{70}, for which the complex with perovskite might not be strong enough and therefore migrates through the layer. This would mean that the strength in which perovskite and fullerene interact in solution might also be transferred to film scenario, and therefore fullerenes with more affinity to perovskite would potentially be able to, for example, passivate defects through more tight non-covalent bonds or complexes that may help the perovskite to crystallize into a higher quality layer.

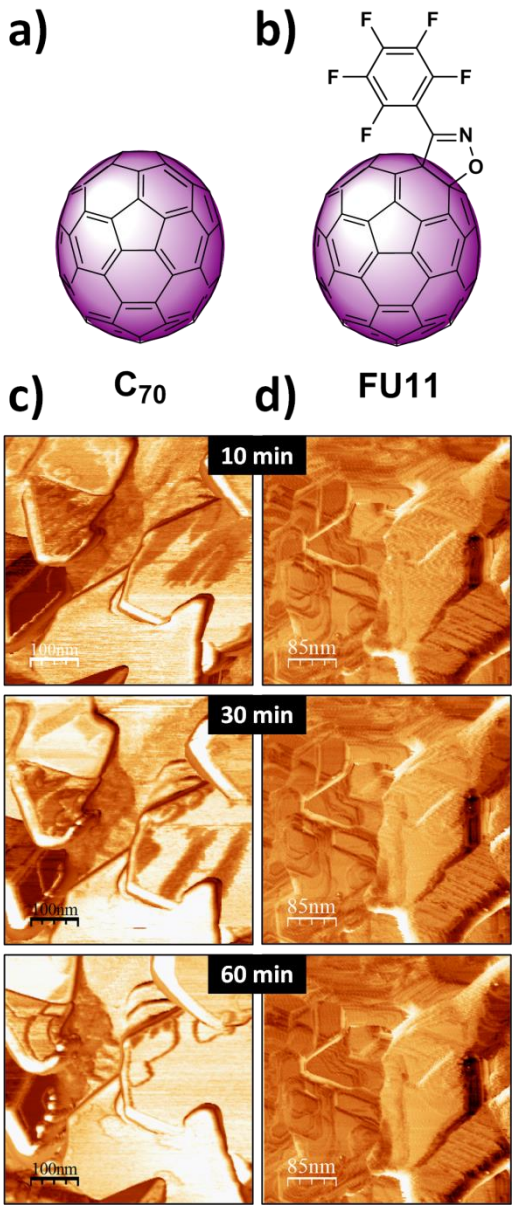

Fig. 3. a) Molecular structure of C_{70}; b) Molecular structure of **FU11**; c) AFM phase images of MAPI:C_{70} and d) MAPI:**FU11** films at different times.

These layers were applied in the fabrication of devices of diverse configurations. In Table 1 the average and maximum values are shown and the distribution of PV parameter values for each of the device configurations is available in Fig. S17-19. First, MAPI layers containing C_{70} and **FU11** were compared to the pristine perovskite in ETL-free devices on fluorine-doped tin oxide (FTO) substrates, with 2,2',7,7'-tetrakis-(*N*,*N*-di-4-methoxyphenylamino)-9,9'-spirobifluorene (spiro-OMeTAD) as HTL and Au as top contact. The whole structure can be seen in the cross-section micrograph acquired by field-emission scanning electron microscopy (FE-SEM) means in Fig. 4a. As proven in literature, the use of fullerenes such as C_{70} inside the perovskite layer greatly improve the quality of films that otherwise would show a high density of pinholes when deposited directly on FTO.[21] In our case, the use of C_{70} helped achieving better PCE values, an effect that was enhanced when

applying **FU11**. This outcome was tried to be reproduced in n-i-p devices with compact and mesoporous TiO_2 (c- and mp-TiO_2, respectively) as ETL (Fig. 4b), but there was not such an improvement but a slight increase in the maximum PCE. Nevertheless, the improvement in the FF was particularly impressive, achieving excellent values up to 81.8% with the use of **FU11** (Fig. S18), which is in agreement with most of perovskite:fullerene blend applications in literature.[25,26,29] Finally, these fullerenes were tried in p-i-n devices, precisely on ITO/PTAA (indium tin oxide/poly[bis(4-phenyl)(2,5,6-trimentlyphenyl)amine]) substrates and with C_{60}/bathocuproine (BCP)/Cu as top contact (Fig. 4c). Cells improved with both fullerenes, moderately with C_{70}-containing films, but with **FU11** a narrow distribution of excellent PCE values was obtained. A record device with a PCE value of 18.3% was obtained, with a short-circuit current density (J_{sc}) of 22.32 mA cm^{-2}, an open-circuit voltage (V_{oc}) of 1061 mV and a FF of 77.3%. These results, which mainly come from the improvement of FF, could have their origin in the possibility of fullerenes to passivate defects. The enhanced ability of **FU11** could be related to the stronger complex that we have earlier proposed that it forms with perovskite. The possibility for **FU11** to bind tightly to perovskite precursors might also favor binding potential defects in the perovskite at the grain boundaries. In this sense, the way in which fullerene interacts with perovskite in the precursor solution might have a great importance, as it might influence the efficiency in which it can improve the film characteristics in terms of defect suppression.

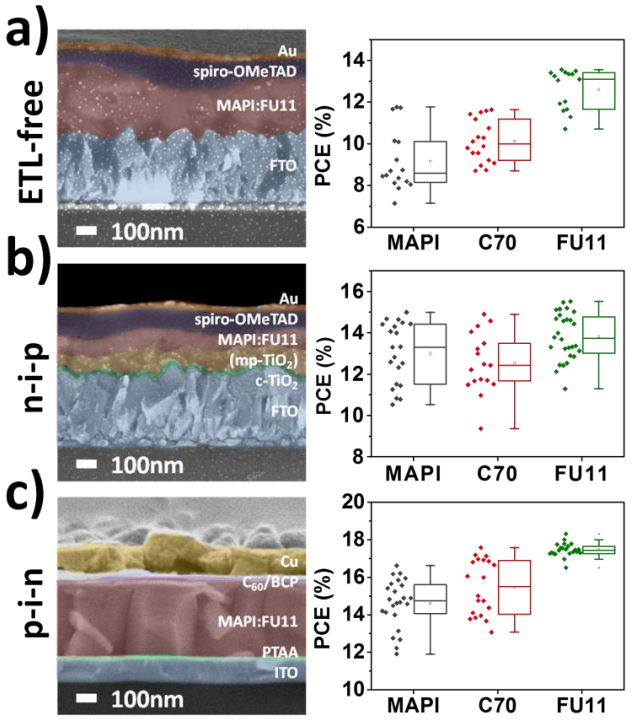

Fig. 4. a) Cross-section micrographies by FE-SEM means and PCE values distribution of ETL-free devices on FTO, b) n-i-p devices on FTO/c-TiO_2/mp-TiO_2 and c) p-i-n devices on ITO/PTAA of MAPI perovskite with C_{70} and **FU11** fullerenes.

Table 1. Average and highest PCE cells (in brackets) PV parameter values of the devices in each of the configurations with MAPI, MAPI:C_{70} and MAPI:**FU11** layers.

	Perovskite layer	J_{sc} [mA cm^{-2}]	V_{oc} [V]	FF [%]	PCE [%]
ETL-free	MAPI	14.4 (16.2)	1.01 (1.08)	62.4 (67.4)	9.2 (11.8)
	MAPI:C_{70}	15.0 (15.1)	1.03 (1.06)	65.5 (73.0)	10.1 (11.6)
	MAPI:**FU11**	16.6 (16.9)	1.05 (1.07)	72.2 (75.1)	12.6 (13.6)
n-i-p	MAPI	17.4 (19.0)	1.03 (1.03)	72.3 (77.0)	13.0 (15.0)
	MAPI:C_{70}	17.0 (19.2)	1.02 (1.04)	72.6 (74.7)	12.5 (14.9)
	MAPI:**FU11**	17.3 (18.9)	1.04 (1.04)	77.0 (78.8)	13.8 (15.5)
p-i-n	MAPI	21.0 (21.7)	0.98 (1.05)	70.7 (73.1)	14.6 (16.6)
	MAPI:C_{70}	21.5 (21.9)	0.99 (1.03)	72.6 (77.9)	15.5 (17.6)
	MAPI:**FU11**	22.1 (22.3)	1.04 (1.06)	76.1 (77.3)	17.5 (18.3)

Fullerene **FU11** worked particularly well in p-i-n devices and showed the highest efficiency values among the different device architectures. We checked the microstructural properties of MAPI:**FU11** layers on PTAA and, as Fig. 5a shows in the top-view and cross-section (in the inset) micrographs, a flat layer with good morphology was achieved, with large grain size distribution of 100-300 nm. Fig. 5b shows the *J-V* curve of the best device for each type of MAPI film, showing again the improvement that the fullerenes bring to p-i-n configuration. Small hysteresis could be observed, which was unchanged for every type of MAPI film. The maximum power point tracking that we can be seen in Fig. 5c revealed a stabilized 18.3% after 2 min at 1 sun of illumination, being a stable value as identical to the original value. In Fig. 5d we present the incident photon-to-photon conversion efficiency (IPCE) spectrum of the best cell. The J_{sc} value that we could integrate from it was 22.22 mA cm^{-2}, which is in perfect agreement with the J_{sc} value of 22.32 mA cm^{-2} obtained from the *J-V* curve.

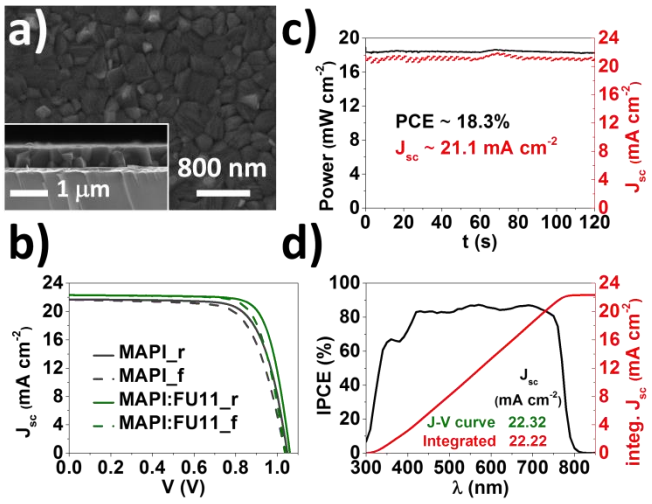

Fig. 5. a) Top-view FE-SEM micrograph of MAPI:**FU11** layer on ITO/PTAA and cross-section in the inset; b) Best *J-V* curves in reverse (r) and forward (f) scan for MAPI and MAPI:**FU11** in p-i-n devices; c) Stabilized power output and short-circuit current density for record device; d) IPCE spectrum and integrated current curve for record device. A comparison between the integrated J_{sc} and the one taken from the *J-V* curve is given.

Conclusion

As a summary, by using a novel combination of spectroscopic techniques we provided further insights into out the working mechanism in which fullerene participates in the perovskite complex in solution, and how its functionalization affects the outcome in the layer and device properties. Fullerenes that showed the ability to form stronger complexes with perovskite might be able to passivate defects in the perovskite film more effectively. With this purpose in mind, a novel, optimized fullerene was designed, which led to highly improved devices with a main enhancement in FF. This strategy was furthermore proven to be universal for many types of devices of different configuration. Deepening in the understanding of the working mechanisms of fullerenes and the relevance of their chemical nature in solution allowed controlling the system from the solution state to device fabrication, going through film properties. This would in turn pave the way for designing structurally advanced fullerenes, searching for a particular behavior in the perovskite solution. In this sense, taking advantage of the knowledge gained with this study, a new fullerene with optimized structure, **FU11**, could be synthesized and applied in blend films with perovskite, achieving efficiencies of up to 18.3% and universality of this technique for different cell configurations. Although there is still a lot to understand about these carbon nanomaterials for perovskite applications, this work sheds light on the next steps for an efficient application of these molecules towards future standard protocols.

Experimental Section

Materials

Chemicals and reagents for synthesis were purchased from commercial suppliers and used as received. All solvents were dried according to standard procedures. Air-sensitive reactions were performed under argon atmosphere. Flash chromatography was performed using silica gel (Merck, Kieselgel 60, 230–240). Analytical thin layer chromatography (TLC) was performed using aluminum coated Merck Kieselgel 60 F254 plates. The materials used in the photovoltaic study were obtained from commercial suppliers in high purity and used without further purification: glass/FTO (TEC15, Hartford Glass), MAI (DYESOL), FAI (DYESOL) $PbCl_2$ (98 %, Sigma–Aldrich), $PbBr_2$ (TCI Chemicals), spiro-OMeTAD (99%, Feiming Chemicals Limited), lithium bis(trifluoromethane) sulfonimidate (LiTFSI, 99.9%, Solvionic), tert-butylpyridine (TBP, 96 %, Sigma–Aldrich), FK209 (Sigma–Aldrich), DMF (extra pure, Scharlab), DMSO (Acros Organics), 2-propanol (synthetic grade, Scharlab), acetone (technical grade, Scharlab), chlorobenzene (99.8%, Sigma–Aldrich) and acetonitrile (UV HPLC grade, Scharlab). For the fabrication of p-i-n devices, anhydrous DMSO, DMF, ethyl acetate and toluene were purchased from Sigma–Aldrich. PTAA, BCP and C_{60} (99.9%) were purchased from Sigma Aldrich. Cu turnings were purchased from Alfa Aesar. MAI was purchased from Dyenamo and PbI_2 from TCI. Patterned indium tin oxide (ITO) glass substrates (25 x 25 mm, 15 Ω sq^{-1}) were purchased from Automatic Research GmbH.

Synthesis and materials

Chemicals were purchased from commercial suppliers and used without further purification. Reactions under nitrogen or argon atmosphere were performed in flame-dried glass ware with dry solvents. For flash chromatography silica gel (40–60 μm) from Acros was used. **FU10** (2,3,4,5,6-pentafluorobenzaldehyde oxime) was synthesized according to a literature procedure.[28] Specific details about **FU11** synthesis (Scheme S1) can be found in the Supporting Information.

Characterization

The morphological properties of the films were analyzed with an ULTRA plus ZEISS FE-SEM. FTIR spectra were obtained with a Nicolet 6700, recording 32 scans with a resolution of 2 cm^{-1} using a liquid cell of 0.1 mm path length with AgCl windows. NMR spectra were recorded on a Bruker Avance 300 (^{1}H: 300.2 MHz, ^{13}C: 75.5 MHz, ^{19}F: 376.4 MHz) at room temperature. The chemical shift (δ) is quoted in ppm relative to the internal standard tetramethylsilane (TMS). Mass spectra were recorded on a Bruker-ULTRAFLEX III (MALDI-TOF) in the facilities of the Universidad Autonoma de Madrid. Fullerene-containing perovskite thin films for AFM measurement were transferred from vacuum darkness conditions to the humidity controlled AFM chamber to avoid degradation. AFM measurements were carried out under N_2 controlled atmosphere (RH<10%) at room temperature using a Nanotec S.L microscope operated in tapping mode with silicon tips (OMCL- C240TS-R3, nominal k = 3 N m^{-1} and f = 70 kHz). Freely available WSxM software has been used for image acquisition and processing.[56]

ETL-free device fabrication

Glass/FTO samples were cleaned by the following procedure: the samples were sonicated in distilled water with soap for 5 min, rinsed thoroughly with distilled water, dried, and sonicated in acetone and 2-propanol for 15 min in each solvent. All the spin-coating layer deposition steps were conducted in a nitrogen atmosphere. The perovskite solution was prepared by dissolving 7.71 mmol of MAI and 2.57 mmol of $PbCl_2$ (molar ratio 3:1) in 3 mL of DMF and stirring overnight. Prior to deposition, perovskite solution was saturated

with the corresponding fullerene. The resulting solution was spin coated on the substrates following a two-step protocol, which consisted of a first step of 500 rpm for 5 s followed by a second step of 2000 rpm for 45 s. Subsequently, the samples were annealed at 100°C for 2 h. On top of the perovskite layer, the spiro-OMeTAD hole-selective contact was deposited from a solution that contained spiro-OMeTAD (108.4 mg) in chlorobenzene (953.4 μL), LiTFSI solution in MeCN (17.17 μL, 520 mg mL^{-1}), and tert-butylpyridine (29.4 μL). The HTL was deposited by spin coating the solution at 3000 rpm for 30 s. The samples were left in a desiccator overnight. Finally, an array of round Au back contacts (~ 0.07 cm^2) was deposited by thermal evaporation at more than 5 x 10^{-6} torr with a NANO38 (Kurt J. Lesker) apparatus with a shadow mask.

ETL-free device characterization

The *J-V* characteristics of the solar cells were measured under a xenon arc lamp simulator equipped with an AM1.5G spectral filter (Sun 2000, ABET Technologies). The intensity was adjusted to provide 1 sun illumination (100 mW cm^{-2}) by using a calibrated silicon solar cell. Unless otherwise mentioned, the *J-V* characteristics were recorded by scanning the potential from higher than the V_{oc} to zero at approximately 300 mV s^{-1}. Before the measurement, a voltage of approximately 1.2 V was applied to the devices for 1 min.

n-i-p device fabrication

Glass/FTO 10 Ω sq^{-1} is cleaned by sonication in 2% Hellmanex water solution for 30 min. After rinsing with water, the substrates are further sonicated with ethanol for another 30 min and, after drying, with acetone for the same amount of time. After a 15 min UV-O_3 treatment, a TiO_2 compact layer is deposited on FTO via spin-coating from a 2 M $TiCl_4$ solution in H_2O. After a 5000 rpm/20 s spin-coating program, the substrates are sintered at 100°C for 10 min. Then, a mesoporous TiO_2 layer is deposited by spin coating for 10 s at 4000 rpm with a ramp of 2000 rpm s^{-1}, using 30 nm particle paste (Dyesol 30 NR-D) diluted in ethanol to achieve 150-200 nm thick layer. After the spin coating, the substrates are sintered with a heating ramp up to 450°C, at which they are left for 30 min under dry air flow. Li-doping of mesoporous TiO_2 is obtained by spin coating a 10 mg mL^{-1} solution of LiTFSI in acetonitrile at 3000 rpm for 10 s. The substrate with Li-doped mesoporous TiO_2 is completed with a second sintering process, the same as before. After cooling down to 150°C the substrates are immediately transferred in a nitrogen atmosphere glove box for deposition of the perovskite films.The perovskite films are deposited from a freshly prepared precursor solution, containing PbI_2:MAI, 1:1 mol/mol, 1.2 M in anhydrous DMSO, either pure or fullerene-saturated. The perovskite solution is spin coated following a two step-program at 1000 and 6000 rpm for 10 and 30 s respectively. During the second step, 150 μL of chlorobenzene are dripped onto the spinning substrate 5 s prior the end of the program. The substrates are then annealed at 100°C for 30 min.

After the perovskite annealing the substrates are allowed to cool down for few minutes and 50 μL spiro-OMeTAD solution (70 mmol in chlorobenzene) are spun at 4000 rpm for 20 s. The HTM solution is doped with TPB (3.3 mol/mol with respect to spiro-OMeTAD), LiTFSI (1.8 M in acetonitrile, 0.5 mol/mol with respect to spiro-OMeTAD) and FK209 (0.25 M in acetonitrile, 0.03 mol/mol with respect to Spiro). Finally, 80 nm gold top electrode is thermally evaporated using a Quorum Q150T, under around 5 x 10^{-5} mbar, through an appropriate shadow mask (0.25 cm^2 pixel).

n-i-p device characterization

The solar cells performances were measured using a Solixon A-20 Solar Simulator. Current-voltage characteristics of the cells were obtained by applying an external voltage bias while measuring the current response with a digital source meter (Keithley 2400). The employed voltage scan rate was 10 mV s^{-1} and no device preconditioning was applied before starting the measurement, such as light soaking or forward voltage bias applied for long time. The cells were masked with a black metal mask (0.16 cm^2) to estimate the active area and reduce the influence of the scattered light.

p-i-n device fabrication

Glass/ITO samples were cleaned by the following procedure: the samples were sonicated in distilled water with soap for 5 min, rinsed thoroughly with distilled water, dried, and sonicated in acetone and 2-propanol for 15 min in each solvent. After that, directly before HTM deposition, substrates were treated in an UV-O_3 cleaner for 15 min.

All the spin-coating layer deposition steps were conducted in a nitrogen atmosphere. PTAA (2 mg mL^{-1} in toluene) was spin-coated (4000 rpm for 30 s) and annealed for 10 min at 100°C on glass/ITO substrates. MAPI perovskite 1.2 M solution was obtained by preparing a 1.5 M nominal MAI solution in DMF:DMSO (6:1 volume ratio) as stock solution and adding the corresponding volume to PbI_2. For perovskite:fullerene blend film preparation, DMF:DMSO mixtures for MAI stock solution contained the corresponding fullerene in 0.05 mg mL^{-1} concentration. A volume of 100 mL of perovskite solution was spread on the substrate one step spin-coating process (4000 rpm for 35 s) was carried out. A volume of 500 mL of ethyl acetate was dripped on the substrate 20 s after the start of the spin-coating process. Subsequently, the samples were annealed at 100°C for 1 h. The substrates were covered by thermally evaporated layers of C_{60} (380°C, 0.15 A s^{-1}) and BCP (140ºC, 0.15 A s-1), with a thickness of 23 nm and 8 nm, respectively. Finally, 80 nm thick Cu metal frame was evaporated as a top contact, defining the active area of 0.144 cm^2.

p-i-n device characterization

Current-voltage characteristics under 1 sun equivalent illumination were recorded using an Oriel LCS-100 class ABB solar simulator in a N_2-filled glovebox, calibrated with a Silicon reference cell from Fraunhofer ISE. The *J-V* curve was acquired with 0.1 V s^{-1} scan rate and a voltage step of 10 mV. The external quantum efficiency (EQE) was measured as a function of wavelength from 300 to 850 nm with a step of 10 nm using a home-built small-spot EQE system. A Stanford Research SR830 Lock-In amplifier is used to measure the electrical response of the device under test and evaluated in TracQ-Basic software.

Conflicts of interest

There are no conflicts to declare.

Acknowledgements

J. P. and S.C. acknowledge Basque Government for a PhD research grant. J. L. D. acknowledges Ikerbasque, the Basque Foundation for Science, for an "Ikerbasque Research Fellow" contract, Polymat Foundation, MINECO of Spain (CTQ2015-71936-REDT) and UPV/EHU (Ayudas a los grupos de investigación de la UPV/EHU).

Notes and references

1 A. Kojima, K. Teshima, Y. Shirai, T. Miyasaka, *J. Am. Chem. Soc*. 2009, **131**, 6050.
2 NREL Best Research-Cell Efficiencies, https://www.nrel.gov/pv/assets/pdfs/best-reserch-cell-efficiencies.pdf, accessed March, 2019.
3 S. Collavini, J. L. Delgado, *Adv. Energy Mater*. 2016, 1601000.
4 T. Gatti, E. Menna, M. Meneghetti, M, Maggini, A. Petrozza, F. Lamberti, *Nano Energy* 2017, **41**, 84.
5 L. L. Deng, S.-Y. Xie, F. Gao, *Adv. Electron. Mater*. 2017, 1700435.
6 Y. Fang, C. Bi, D. Wang, J. Huang, *ACS Energy Lett.* 2017, **2**, 782.
7 E. Castro, J. Murillo, O. Fernandez-Delgado, L. Echegoyen, *J. Mater. Chem. C* 2018, **6**, 2635.
8 A.-N. Cho, N.-G. Park, *ChemSusChem* 2017, **10**, 3687.
9 C.-Y. Chang, W.-K. Huang, Y.-C. Chang, K.-T. Lee, C.-T. Chen, *J. Mater. Chem. A* 2016, **4**, 640.
10 X. Liu, W. Jiao, M. Lei, Y. Zhou, B. Song, Y. Li, J. Mater. Chem. A 2015, 3, 9278.
11 P. Docampo, J. M. Ball, M. Darwich, G. E. Eperon, H. J. Snaith, *Nat. Commun*. 2013, **4**, 2761.
12 J. Y. Jeng, K. C. Chen, T. Y. Chiang, P. Y. Lin, T. D. Tsai, Y. C. Chang, T. F. Guo, P. Chen, T. C. Wen, Y. J. Hsu, *Adv. Mater.* 2014, **26**, 4107.
13 Y. Bai, Q. Dong, Y. Shao, Y. Deng, Q. Wang, L. Shen, D. Wang, W. Wei, J. Huang, Nat. Commun. 2016, 7, 12806.
14 H. Azimi, T. Ameri, H. Zhang, Y. Hou, C. O. R. Quiroz, J. Min, M. Hu, Z.-G. Zhang, T. Przybilla, G. J. Matt, E. Spiecker, Y. Li, C. J. Brabec, *Adv. Energy Mater.* 2015, **5**, 1401692.
15 C. Tian, K. Kochiss, E. Castro, G. Betancourt-Solis, H. Han, L. Echegoyen, *J. Mater. Chem. A* 2017, **5**, 7326.
16 Q. Xue, Y. Bai, M. Liu, R. Xia, Z. Hu, Z. Chen, X.-F. Jiang, F. Huang, S. Yang, Y. Matsuo, H.-L. Yip, Y. Cao, *Adv. Energy Mater*. 2017, **7**, 1602333.
17 S. Collavini, I. Kosta, S. F. Völker, G. Cabanero, H. J. Grande, R. Tena-Zaera, J. L. Delgado, *ChemSusChem* 2016, **9**, 1263.
18 W. Ke, D. Zhao, C. R. Grice, A. J. Cimaroli, J. Ge, H. Tao, H. Lei, G. Fang, Y. Yan, *J. Mater. Chem. A* 2015, **3**, 17971.
19 Y. Li, Y. Zhao, Q. Chen, Y. M. Yang, Y. Liu, Z. Hong, Z. Liu, Y.-T. Hsieh, L. Meng, Y. Li, Y. Yang, *J. Am. Chem. Soc.* 2015, **137**, 15540.
20 Z. Wang, D. P. McMeekin, N. Sakai, S. van Reenen, K. Wojciechowski, J. B. Patel, M. B. Johnston, H. J. Snaith, *Adv. Mater.* 2017, **29**, 1604186.
21 J. Pascual, I. Kosta, T. T. Ngo, A. Chuvilin, G. Cabanero, H. J. Grande, E. M. Barea, I. Mora-Seró, J. L. Delgado, R. Tena-Zaera, *ChemSusChem* 2016, **9**, 2679.
22 J. Xu, A. Buin, A. Ip, W. Li, O. Voznyy, R. Comin, M. Yuan, S. Jeon, Z. Ning, J. J. McDowell, P. Kanjanaboos, J.-P. Sun, X. Lan, L. N. Quan, D. H. Kim, I. G. Hill, P. Maksymovych, E. Sargent, *Nat. Commun.* 2015, **6**, 7081.
23 K. Wang, C. Liu, P. Du, J. Zheng, X. Gong, *Energy Environ. Sci.* 2015, **8**, 1245.
24 M. Li, Y.-H. Chao, T. Kang, Z.-K. Wang, Y.-G. Yang, S.-L. Feng, Y. Hu, X.-Y. Gao, L.-S. Liao, C.-S. Hsu, *J. Mater. Chem. A* 2016, **4**, 15088.
25 X. Liu, F. Lin, C.-C. Chueh, Q. Chen, T. Zhao, P.-W. Liang, Z. Zhu, Y. Sun, A. K.-Y. Jen, *Nano Energy* 2016, **30**, 417.
26 F. Zhang, W. Shi, J. Luo, N. Pellet, C. Yi, X. Li, X. Zhao, T. J. S. Dennis, X. Li, S. Wang, Y. Xiao, S. M. Zakeeruddin, D. Bi, M. Grätzel, *Adv. Mater.* 2017, **29**, 1606806.
27 S. Collavini, M. Saliba, W. R. Tress, P. J. Holzhey, S. F. Völker, K. Domanski, S.-H. Turren-Cruz, A. Ummadisingu, S. M. Zakeeruddin, A. Hagfeldt, M. Grätzel, J. L. Delgado, *ChemSusChem* 2018, **11**, 1032.
28 R. Sandoval-Torrientes, J. Pascual, I. García-Benito, S. Collavini, R. Tena-Zaera, N. Martín, J. L. Delgado, *ChemSusChem* 2017, **10**, 2023.
29 Y. Shao, Z. Xiao, C. Bi, Y. Yuan, J. Huang, *Nat. Commun*. 2014, **5**, 5784.
30 Y. Zhao, J. Wei, H. Li, Y. Yan, W. Zhou, D. Yu, Q. A. Zhao, *Nat. Commun*. 2016, **7**, 10228.
31 Z. Xiao, C. Bi, Y. Shao, Q. Dong, Q. Wang, Y. Yuan, C. Wang, Y. Gao, J. Huang, *Energy Environ. Sci*. 2014, **7**, 2619.
32 H. J. Snaith, A. Abate, J. M. Ball, G. E. Eperon, T. Leijtens, N. K. Noel, S. D. Stranks, J. T.-W. Wang, K. Wojciechowski, W. Zhang, *J. Phys. Chem. Lett.* 2014, **5**, 1511.
33 X. Sun, L. Y. Li, W. W. Chen, X. Guo, H. H. Wang, M. Lei, Q. Wang, Y. F. Li, *J. Mater. Chem. A* 2017, **5**, 20720.
34 C. Liu, W. Li, H. Li, C. Zhang, J. Fan, Y. Mai, *Nanoscale* 2017, **9**, 13967.
35 M. Jung, S.-G. Ji, G. Kim, S. I. Seok, *Chem. Soc. Rev*. 2019, **48**, 2011.
36 N. Ahn, D.-Y. Son, I.-H. Jang, S. M. Kang, M. Choi, N.-G. Park, *J. Am. Chem. Soc.* 2015, **137**, 8696.
37 J.-W. Lee, H.-S. Kim, N.-G. Park, *Acc. Chem. Res*. 2016, **49**, 311.
38 X. Guo, C. McCleese, C. Kolodziej, A. C. S. Samia, Y. Zhao, C. Burda, *Dalton Trans.* 2016, **45**, 3806.
39 L. Zhi, Y. Li, X. Cao, Y. Li, X. Cui, L. Ci, J. Wei, *Nanoscale Res. Lett.* 2017, **12**, 632.
40 Q. Hu, L. Zhao, J. Wu, K. Gao, D. Luo, Y. Jiang, Z. Zhang, C. Zhu, E. Schaible, A. Hexemer, C. Wang, Y. Liu, W. Zhang, M. Grätzel, F. Liu, T. P. Russell, R. Zhu, Q. Gong, *Nat. Commun*. 2017, **8**, 15688.
41 J.-W. Lee, Z. Dai, C. Lee, H. M. Lee, T.-H. Han, N. De Marco, O. Lin, C. S. Choi, B. Dunn, J. Koh, D. Di Carlo, J. H. Ko, H. D. Maynard, Y. Yang, *J. Am. Chem. Soc*. 2018, **140**, 6317.
42 M. Yavari, M. Mazloum-Arkadani, S. Gholipour, N. Marinova, J. L. Delgado, S.-H. Turren-Cruz, K. Domanski, N. Taghavinia, M. Saliba, M. Grätzel, A. Hagfeldt, W. Tress, *Adv. Energy Mater*. 2018, **8**, 1702719.
43 S. Gharibzadeh, F. V. A. Camargo, C. Roldán-Carmona, G. C. Gschwend, J. Pascual, R. Tena-Zaera, G. Cerullo, G. Grancini, M. K. Nazeeruddin, *Adv. Mater.* 2018, **30**, 1801496.
44 B. L. Schottel, H. T. Chifotides, K. Dunbar, *Chem. Soc. Rev.* 2008, **37**, 68.
45 B. P. Hay, V. S. Bryantsev, *Chem. Commun*. 2008, 2417.
46 A. Frontera, P. Gamez, M. Mascal, T. J. Mooibroek, J. Reedijk, *Angew. Chem. Int. Ed.* 2011, **50**, 9564.
47 H. T. Chifotides, K. R. Dunbar, *Acc. Chem. Res.* 2016, **46**, 894.
48 R. E. Dawson, A. Hennig, D. P. Weimann, D. Emery, V. Ravikumar, J. Montenegro, T. Takeuchi, S. Gabutti, M. Mayor, J. Mareda, C. A. Schalley, S. Matile, *Nat. Chem.* 2010, **2**, 533.
49 M. Giese, M. Albrecht, K. Rissanen, *Chem. Commun.* 2016, **52**, 1778.
50 C.-Z. Li, C.-C. Chueh, F. Ding, H.-L. Yip, P.-W. Liang, X. Li, A. K.-Y. Jen, *Adv. Mater*. 2013, **25**, 4425.
51 X. Sun, W. Chen, L. Liang, W. Hu, H. Wang, Z. Pang, Y. Ye, X. Hu, Q. Wang, X. Kong, Y. Jin, M. Lei, *Chem. Mater.* 2016, **28**, 8726.
52 J. L. Delgado, E. Espíldora, M. Liedtke, A. Sperlich, D. Rauh, A. Baumann, C. Deibel, V. Dyakonov, N. Martín, *Chem. Eur. J.* 2009, **15**, 13474.
53 C. Villegas, M. Wolf, D. Joly, J. L. Delgado, D. M. Guldi, N. Martín, *Org. Lett.* 2015, **17**, 5056.

54 M. Wolf, C. Villegas, O. Trukhina, J. L. Delgado, T. Torres, N. Martín, T. Clark, D. M. Guldi, *J. Am. Chem. Soc*. 2017, **139**, 17474.
55 J. Pascual, I. Kosta, E. Palacios-Lidon, A. Chuvilin, G. Grancini, M. K. Nazeeruddin, H. J. Grande, J. L. Delgado, R. Tena-Zaera, *J. Phys. Chem. C* 2018, **122**, 2512.
56 I. Horcas, R. Fernandez, J. M. Gomez-Rodriguez, J. Colchero, J. Gomez-Herrero, A. M. Baro, *Rev. Sci. Instrum.* 2007, **78**, 013705